Original Article

Institution of MECHANICAL ENGINEERS
Journal of AEROSPACE ENGINEERING

Proc IMechE Part G:
J Aerospace Engineering
2023, Vol. 237(4) 853–864

DOI: 10.1177/09544100221111305
journals.sagepub.com/home/pig
SAGE

Effect of the trailing-edge flap on tones due to self-excited oscillation within the leading-edge slat cove

Weishuang Lu[1,2,3,4], Peiqing Liu[1,2,3] and Hao Guo[1,2,3]

Abstract

To study the tonal noise characteristics of the leading-edge slat of high-lift configurations with and without a deployed trailing-edge flap, experiments are conducted in the D5 aero-acoustic wind tunnel at Beihang University. The numerical simulation method is used to obtain the necessary flow information. The experimental results show that low to mid frequency tonal noise generated by self-excited oscillation within the slat cove is dominant and its corresponding frequencies are basically unchanged whether the flap is deployed or not. However, the primary mode of self-excited oscillation within the slat cove switches to a higher one when the flap is deployed. Further analysis results demonstrate that variation of the primary mode is found to be closely related to the flow characteristics in the self-excited oscillation feedback loop. The number of the primary mode is generally proportional to the ratio between the vortex shedding frequency and the self-excited oscillation frequency. The flap being deployed results in an increase in the effective angle of attack of both the main wing and slat, which leads to a thinner separating boundary layer, thus increasing further the vortex shedding frequency and this ratio.

Keywords

high-lift device, leading-edge slat, aerodynamic noise, acoustic characteristics, trailing-edge flap

Date received: 18 January 2022; accepted: 9 May 2022

Introduction

Airframe noise is a significant contributor to the overall noise of a plane in the approach and landing phases.[1,2] The level of aero-acoustic noise generated by airframe sources may be comparable to that of engine noise.[1] In particular, the leading-edge slat has been regarded as a major noise source[3,4] for regional, short range jets.

Recently, a considerable amount of experimental[5,6] and numerical[7–9] work has been devoted to aero-acoustics noise research regarding slats. Three main elements have been identified in the context of slat generated noise, including low to mid frequency broadband noise[10] due to the turbulent kinetic energy in the recirculation zone, tonal noise superimposed on the low-frequency broadband noise[6,10] generated by the self-excited oscillation within the slat cove, and high-frequency hump noise caused by trailing-edge vortex shedding.[11] Among such noise components, low-frequency tonal noise is a significant contributor to the overall noise, and much research[5,9] has been carried out on the noise characteristics regarding low-frequency tonal noise. In order to isolate slat noise from other possible sources, such as the trailing-edge flap, two-element high-lift configurations are used as research objects, that is, the flaps are stowed.[7,12,13]

A 2D model with a deployed slat and retracted flap was designed by Kolb et al.[12] to study the noise sources originating from the leading-edge slat and noise reduction effect of slat cove filler fairings. Experimental results show that the tonal frequency generated by the slat cove flow agrees with frequencies predicted by an analytical formula derived by Rossiter.[14] A high-lift configuration with the deployed slat, separation adapted cove filler and retracted flap was shown with almost equivalent noise emission to a clean configuration with a retracted slat at comparable lift. In addition, Terracol et al.[13] studied the self-excited oscillation phenomenon within the slat cove and deduced its frequency prediction formula by calculating and analyzing the flow field characteristics near the slat of a two-element high-lift configuration. The equation,[13] improving upon Rossiter's original formula,[14] was proposed

[1] Key Laboratory of Aero-Acoustics (Beihang University), Ministry of Industry and Information Technology, Beijing, China
[2] Key Laboratory of Fluid Mechanics (Beihang University), Ministry of Education, Beijing, China
[3] School of Aeronautic Science and Engineering, Beihang University, Beijing, China
[4] Institute of Mechanics, Chinese Academy of Sciences, Beijing, China

Corresponding author:
Hao Guo, Institute of fluid mechanics, Beihang University, Beijing 100191, China.
Email: guohao@buaa.edu.cn

to predict the low-frequency band tonal noise, relying on the time coupling between the vortices convected from the cusp to the reattachment position and sound waves propagated from the reattachment position to the cusp. This equation was applied to many subsequent studies.[15,16] Compared with the three-element high-lift configurations, the two-element high-lift configurations are designed to eliminate the interference of the flap noise. However, their flow fields have a significant difference.[17] The leading-edge and trailing-edge high-lift devices are normally deployed at the same time. Therefore, the three-element high-lift configurations are selected as research objects for recent research work on slat noise.[6,9,18,19] These scholars have studied the effects of different incoming flow conditions,[9] different geometric parameters,[6,18] and different experimental conditions[19] on slat noise. These previous works basically clarified the noise generation mechanism and noise characteristics of the low-frequency tonal noise of the slat cove.

However, the effect of the trailing-edge flap on the noise characteristics of the leading-edge slat has been ignored. Clearly, whether the trailing-edge flap is deployed or not has an influence on the aerodynamic performance of the high-lift configuration,[17] which changes the flow regime near the main wing and slat, and further gives rise to a local effective angle of attack (AoA) of the main wing as well as the leading-edge slat. Briefly, there are significant differences in the aerodynamic noise characteristics of the leading-edge slat according to whether the trailing-edge flap is deployed or not. It is necessary to study the noise characteristics of the leading-edge slat of high-lift configurations with and without a deployed trailing-edge flap, establish a far-field noise characteristics relationship between these two. Accordingly, an experimental study on the aerodynamic noise characteristics of a two-dimensional high-lift configuration model with and without trailing-edge flap at different AoAs in the D5 aero-acoustic wind tunnel at Beihang University is presented in this paper. The corresponding flow characteristic parameters are investigated through the application of a numerical simulation method.

The paper is organized as follows. The *Methodology* section describes the methodology, including the experimental setup and numerical simulations. The *Equations* section presents and discusses the experimental and computational results, whilst a summary of the findings is provided in the *Results and discussion* section along with the conclusion.

Methodology

Experimental setup

Aero-acoustic measurements were conducted in the D5 aero-acoustic wind tunnel at Beihang University, which is a newly commissioned small-scale, closed-circuit aerospace wind tunnel. The test section is 2.5 m in length with a square cross section of 1.0 m by 1.0 m. It is surrounded by an anechoic chamber to provide the non-reflecting condition. The anechoic chamber is 7 m(L) × 6m (W) × 6m(H), with a low cut-off frequency of f = 200 Hz.[20]

To fulfill both the aerodynamic and acoustic measurements of the high-lift configuration, the closed test section with semi-anechoic sidewalls was used in this paper, as shown in Figure 1(a), which is similar to the Virginia Tech Anechoic Wind Tunnel.[21] The sidewall on the suction side consists of a DSM cloth tensioned with a sound-absorbing plate, while the sidewall on the pressure side is just a layer of DSM cloth. When sound waves pass through the DSM cloth[22] and the jet boundary layer,[21] acoustic loss happens. The losses have been measured to correct the measured far-field sound pressure signals. The following results of the Sound Pressure Level (SPL) have been corrected with DSM cloth and boundary layer losses.[23]

As shown in Figure 1(a), far-field microphone and a microphone array are used as sound field measuring equipment. It should be noted that all the acoustic experimental instruments are located at the pressure side of model, as in a flyover configuration, as shown in Figure 1(a), and their relative positions are shown in Figure 1(b). The red dots represent the relative position of 32 microphones of the array, whilst the blue one pertains to the relative position of the free-field microphone.

Far-field noise is measured using the Brüel & Kjær 12-channel acoustic vibration analysis system, which includes a 12-channel compact LAN-XI module and 1/2-inch free-field microphones (type 4189). The free-field microphone sensitivity is 50mV/Pa, and the dynamic range is 14.6dB–146dB. The acoustic signal is measured over a time interval of 41.75s at a sampling frequency of 65,536 Hz. The far-field microphone is placed at 2m distance from the geometric center of the experimental model with a direction angle of 290°.

The microphone array is the KeyGo Tech multi-channel sound source localization system. It consists of 32 1/4-inch free-field microphones distributed spirally within a circle of 1m in diameter. The microphones have a wide frequency range of 20 kHz and the dynamic range extends from 32dB(A) to 135dB. In the present study, acoustic signals were measured at a sampling frequency of 25.6 kHz with time intervals of 10s. Acoustic data were processed at a particular frequency by the conventional beamforming algorithm. The microphone array was also placed at 2m distance from the geometric center of the experimental model with a direction angle of 270°.

A two-dimensional three-element high-lift model is used as the experimental model in this paper, which is manufactured in aluminum alloy with 0.4 m stowed chord length and 1m span length. The geometrical settings of high-lift configuration are described in Table 1, where C represents the stowed chord length. The geometric center of the experimental model is 1m from the nozzle, as shown in Figure 1, and the experimental model is mounted vertically between two end-plates to ensure that the flow around the airfoil is two dimensional. Figure 2 shows a schematic diagram of the geometric profiles of the tested high-lift configuration in this paper.

Measurements were conducted at a freestream velocity of U_∞=50 m/s corresponding to Reynolds numbers based on the airfoil stowed chord of Re_c =1.35 × 10^6. The angle

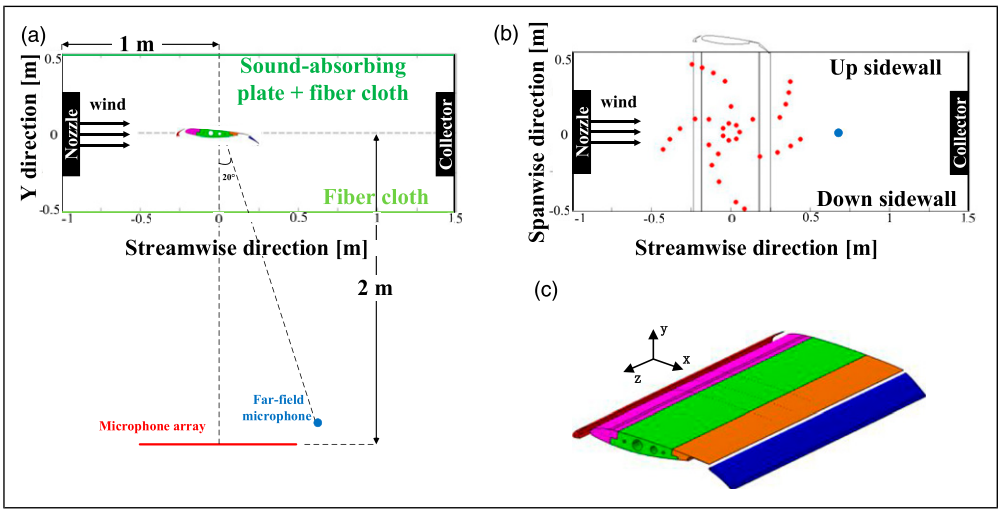

Figure 1. Wind tunnel closed test section and model: (a) Top view of closed test section; (b) Side view of closed test section; (c) Schematic of experimental model.

Table 1. Geometrical settings of the high-lift configuration.

Configuration	Deflection [°]	Gap [%C]	Overlap [%C]	Chord length [%C]
Slat	25	3.25	−2.00	17.8
Flap	32	1.61	0.77	18

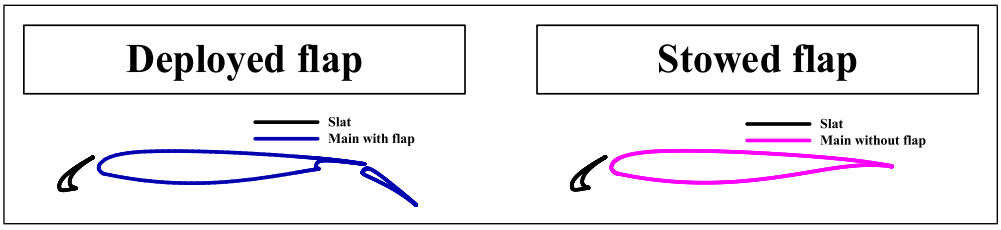

Figure 2. The geometrical profiles of the tested high-lift configuration (left: the configuration with a deployed flap; right: the configuration with a stowed flap).

of attack was from 1° to 10° with an interval of 1°. For the two-element configuration, since the trailing-edge flap is stowed, the effective angle of attack of the high-lift configuration is negative when the AoA is smaller. There is a large separation zone on the pressure surface, which results in an unstable flow regime. Hence, the noise data at small AoAs (below 3°) were discarded and no further analysis performed.

Numerical simulation

Numerical simulation is always carried out as a common method for predicting and analyzing the flow field.[24,25] It needs the assistance of numerical calculation results to analyze the flow field. In this paper, the 2D structured grid is created by the grid generation software ANSYS ICEM and the first-layer grid height of the wall is $1 \times 10-5$ times the reference chord length. The computational fluid dynamics software FLUENT is applied as the solver to simulate the steady incompressible RANS equations and the S-A turbulence model. The two-order upwind schemes are used in the equation of the momentum and turbulent kinetic energy. The pressure–velocity coupling is dealt with by the SIMPLEC algorithm 28. Numerical simulation verification is carried out on Cp, CL of a 30P30P airfoil and its velocity profiles, which have been explained in detail by Ref. 26, are only given a brief overview here.

Figure 3(a) and Figure 3(b) show a comparison of the lift coefficient CL and pressure-coefficient distributions obtained in numerical simulation with the wind tunnel test results, respectively. The results of the numerical simulation are basically in good agreement with the experimental ones in Ref. 27.

It can be observed from Figure 3(c) that the maximum slope of the computed velocity profiles agrees well with the measured data and calculation results in Ref. 28, whilst

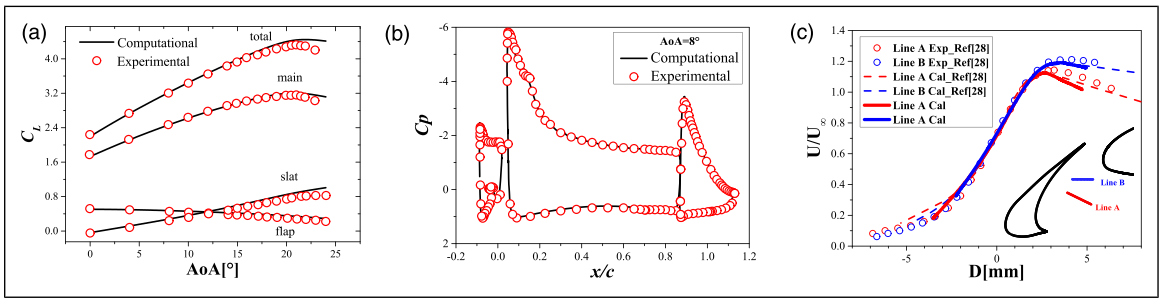

Figure 3. Comparison of the results obtained through numerical simulation with those from the wind tunnel test: (a) Lift coefficient, CL; (b) Pressure coefficient, Cp; (c) Velocity profiles (AoA: Angle of attack, U is the velocity, U_∞ is the freestream velocity).[27,28]

Table 2. Flow field parameter definitions.

Symbol	Parameter definition
L_v	Shear layer length between the cusp and the reattachment position
L	Distance between the separation and reattachment position
δ	Separating boundary layer thickness
U_v	Average convection velocity along the shear layer
U_{max}	Maximum velocity in the separating boundary layer near the cusp
U_∞	Freestream velocity

the maximum velocity in the shear layer is also basically consistent with the experimental data.

Equations

Empirical formula for characteristic frequency prediction

According to the principle of self-excited oscillation within the slat cove,[13] the period of cove self-excited oscillation is derived and is expressed as in the following:

$$T = \frac{L_v}{U_v} + \frac{L}{c} \tag{1}$$

where c is the speed of sound in the air, 340 m/s in this paper, and the other parameters are provided in Table 2. Then, the characteristic frequencies of tonal noise in the low to mid frequency band are expressed as

$$f_n = \frac{n}{\frac{L_v}{U_v} + \frac{L}{c}} = \frac{n}{\frac{L_v}{U_{max} * K_v} + \frac{L}{c}} \tag{2}$$

where $K_v = U_v/U_{max}$, U_{max} is the local incoming velocity at the cusp of the slat cove. It should be noted that n is the quantity of vortices in the shear layer, which also represents the number of self-excited oscillation modes. More local flow field information of the slat cove, such as U_{max}, is considered in equation (2), compared with the empirical formula (shown in equation (3)) derived by M. Terracol et al.[13]

$$f_n = \frac{U_\infty}{L} \frac{n}{(\alpha_L/K_v + Ma)} \tag{3}$$

where $K_v = \frac{U_v}{U_\infty}$, $\alpha_L = \frac{L_v}{L}$.

Flow filed parameters possibly related to the main mode

As mentioned above, the quantity of vortices, n, is that which can be contained simultaneously in the shear layer during a self-excited oscillation period, which also represents the number of modes. The quantity of vortices, n, is related to the flow characteristics in the self-excited oscillation feedback loop, including the shedding characteristics of the vortex near the cusp, motion characteristics of vortex in the free shear layer and the quantity of vortices interacting with the solid surface of the upper trailing edge of the slat within an oscillation period.[29]

According to previous studies on the conventional cavity self-excited oscillation,[30,31] the ratio of the cavity length over the thickness of the separating boundary layer, L/δ, participates in the primary mode selection. In other words, the value of n is determined by this ratio.

For the slat cove, the characteristic frequencies of shedding vortex near the cusp can be expressed as[32]

$$f_v \propto \frac{U_{max}}{\delta} \tag{4}$$

where δ is the characteristic size of the shedding vortex, U_{max} is the maximum velocity in the separating boundary layer near the cusp.

Due to the intermittency of the shear layer, multiple self-excited oscillation modes apparently coexist. The self-excited oscillation may exist in more than one state, shifting between the different modes. The oscillation mode with the strongest noise amplitude can be considered as the primary mode. Hence, n_p, the number of the primary mode can be expressed as

$$n_p \propto \frac{f_v}{f_c} \propto \frac{U_{max}/\delta}{\frac{U_{max} \cdot K_v}{L_v}} \propto \frac{L_v}{\delta \cdot K_v} = \frac{L_v}{\delta \cdot K_v} \tag{5}$$

where f_c is almost equal to f_n, with an n of 1 and among which, L/c is ignored for the reason that, under the tested condition, the time for sound waves traveling to the cusp is

much less than that for the shedding vortex moving to the reattachment position along the shear layer. It is clear that the convection velocity, U_v, within the slat cove is more easily affected by the geometric parameters compared with the conventional cavity. K_v also participates in the primary mode selection of self-excited oscillation within the slat cove. These three flow parameters, L_v, δ and K_v participate in the primary mode selection. The variation law of these three parameters and n when the trailing-edge flap is deployed or not will be discussed in the next subsection.

Results and discussion

Noise spectral characteristics of the three-element high-lift configuration

As shown in Figure 4, there is some tonal noise superimposed on the low to mid frequency broadband noise when the AoA is below 6°. The frequency range corresponding to the tones varies slightly with increasing AoA. As the AoA increases to 7°, broadband noise is dominant. To analyze further the noise characteristics, sound source localization analysis is performed at AoAs of 4° and 7.

The sound source maps are at the frequencies of 1 kHz, 3 kHz, and 8 kHz, respectively. The. Acoustic data are processed at a particular frequency by the conventional beamforming algorithm. As shown in Figure 5, sound source location is in the vicinity of the leading-edge slat at each analysis frequency. On the basis of previous research results, the model noise in these experiments may be generated by the self-excited oscillation within the slat cove.

As shown in Figure 6, the horizontal coordinate is dimensionless, using f_c that is equal to f_n with an n of 1. The spectra from Figure 6 demonstrate that the frequencies corresponding to low to mid frequency tonal noise are basically at where f/f_c is an integer. This can also be seen from Table 3, the comparison between the experimental results and the results calculated from equation (2) for the self-excited oscillation frequencies of the slat cove. As can be seen from Figure 6 and Table 3, ModeI noise (at f_1) is not obvious, ModeII noise (at f_2) is the most obvious, followed by ModeIII noise (at f_3). In addition, the frequencies corresponding to the 2nd peak obtained by the experiment are mostly in good agreement with the self-excited oscillation characteristic frequencies calculated from equation (2), except when the AoA is 4°. When the AoA is less than 7°, frequencies corresponding to the 3rd peak also fits well, and the difference between the two is less than 1% of the empirical value. These demonstrate further that the generation mechanism of noise measured in these experiments is due to the self-excited oscillation within the slat cove.

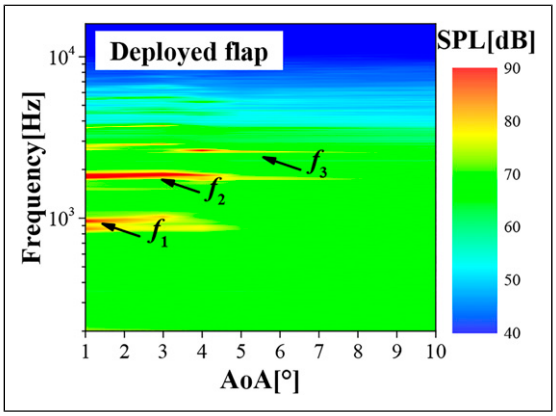

Figure 4. Sound Pressure Level contour map of far-field noise for the three-element high-lift configuration at a freestream velocity of 50 m/s (experimental results).

Furthermore, it can be seen from Figure 6 that the amplitude corresponding to the 2nd peak is significantly higher than that for the 3rd at an angle of attack below 3°. As the angle of attack reaches 4°, the amplitude corresponding to the 2nd peak is already lower than that for the 3rd. In other words, the main characteristic frequency of the self-excited oscillation within the slat cove is initially at f_n, with an n of 2 at smaller AoAs, and switches to f_n, with an n of 3 as the angle of attack increases. The primary mode of the self-excited oscillation switches to a higher one as the AoA increases.

Comparison of far-field noise characteristics for high-lift configurations

In this subsection, a comparison of the far-field noise characteristics between high-lift configurations when the trailing-edge flap is deployed and stowed is made.

Whether the trailing-edge flap is deployed or not, there is some tonal noise produced by the self-excited oscillation in the SPL contour maps, as shown in Figure 7. It can be seen that whether the flap is deployed or not does not substantially affect the corresponding frequencies of the low to mid frequency tonal noise. In addition, the maximum intensity of these tones is basically at the same level, and hence, whether the flap is deployed or not has little effect on the maximum tones intensity. Furthermore, broadband noise also has basically the same level of intensity at the same AoA, which can also be observed in Figure 8.[33]

Figure 8 shows normalized spectra of the high-lift configuration with and without a flap. Similar to Figure 6, the horizontal coordinate is dimensionless. On the one hand, for the high-lift configuration with a deployed flap (navy lines) mentioned in the last subsection, the primary mode of self-excited oscillation switches from Mode IIto Mode IIIas the AoA increases. On the other hand, for the high-lift configuration with a stowed flap (pink lines), at an AoA below 6°, its noise amplitude corresponding to the 2nd peak is significantly higher than that for the 3rd peak. That is, ModeIIis the primary self-excited oscillation mode. While the amplitudes corresponding to the two peaks are basically equal at an AoA of 7°, which can be regarded as the transition phase of ModeIIand ModeIII. When the AoA becomes 8°, the amplitude corresponding to the 2nd peak is already lower than that for the 3rd peak and Mode III is the primary self-excited oscillation mode.

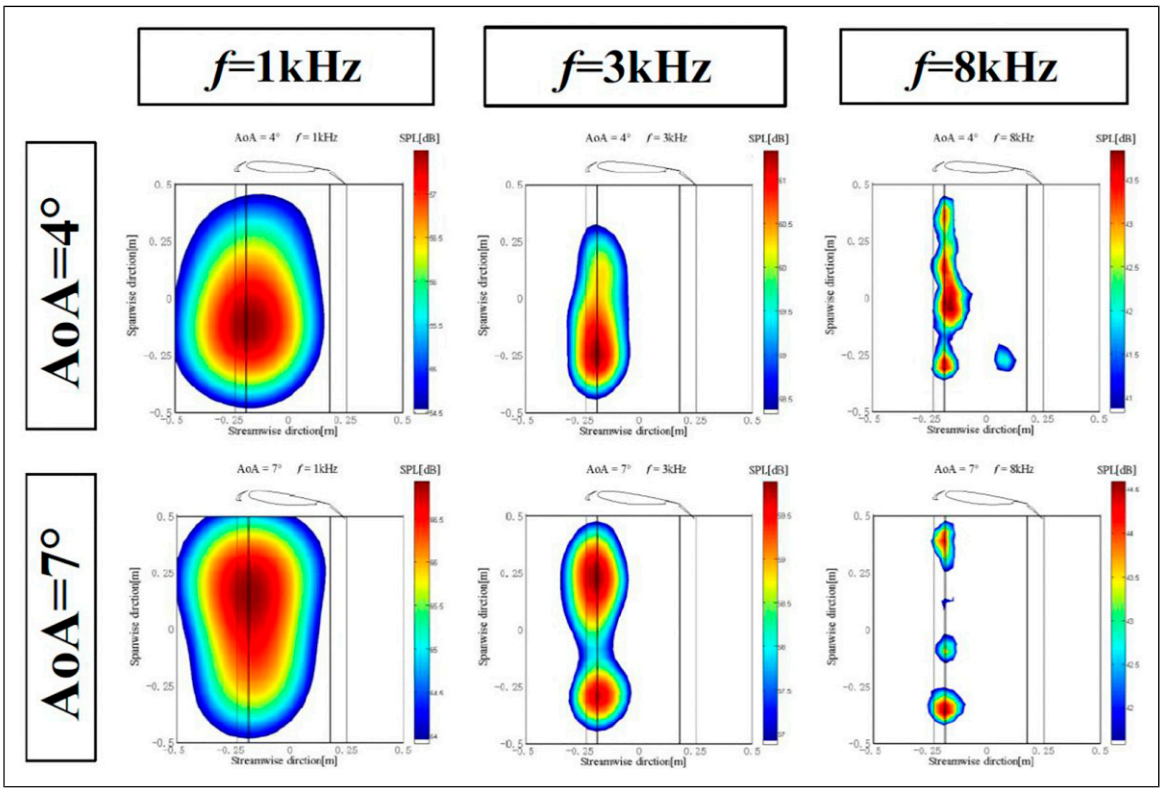

Figure 5. Microphone array noise source maps obtained by the experiment in this paper.

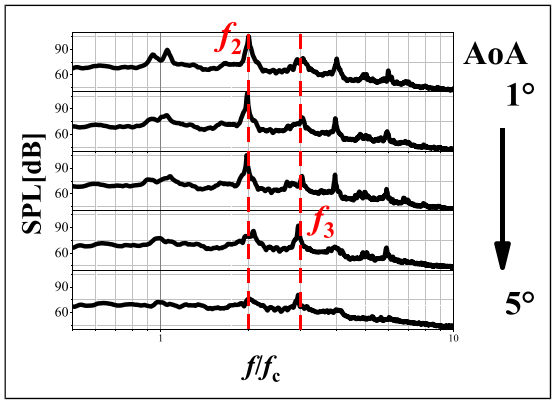

Figure 6. Sound Pressure Level spectrum (in Figure 4) with dimensionless horizontal coordinate (experimental results).

It can be seen that at the same AoA (from 4° to 6°), ModeIIis the main self-excited oscillation mode for the high-lift configuration when the flap is stowed. However, ModeIII is the main self-excited oscillation mode for the high-lift configuration with a deployed flap. Over a certain AoA range, whether the flap is deployed or not changes the value of n. The primary mode of self-excited oscillation within the slat cove switches to a higher one when the flap is deployed.

Effect of the trailing-edge flap on the main mode of self-excited oscillation

As shown in Figure 9, at the same AoA, the position of the stagnation point of the slat moves significantly from the front edge of the upper surface to the cusp of the slat, and the reattachment point of the flow is far away from the trailing edge of the slat, when the flap is deployed. Apart that, due to the flap deployment, the acceleration effect of the gap between the main wing and the slat is more obvious, so that the size of the recirculation zone is significantly reduced. Similar results can also been seen from Figure 10, which shows the pressure distribution of the slat. It can be seen from Figure 10 that the upper surface of the slat provides positive pressure when the flap is stowed, and when the flap is deployed, the upper surface provides negative pressure. These demonstrate that the effective AoA of the incoming flow increases, when the flap is deployed.

Due to the increase in the effective AoA when the flap is deployed, the velocity magnitude at the front edge of the main wing of the high-lift configuration is larger than for the high-lift configuration with a stowed flap at the same AoA. This leads to a higher pressure gradient in the gap between the slat and the main wing. Due to this higher pressure gradient, the mean flow streamline following the mean shear layer near the cusp is closer to the recirculation

Table 3. Comparison between experimental results of characteristic frequencies and empirical formula results(△ is the difference between the experimental value and the empirical value(equation (2)).

	f_n(n=1) [Hz]			f_n(n=2) [Hz]			f_n(n=3) [Hz]		
AoA [°]	Equation (2)	Exp	Δ	Equation (2)	Exp	Δ	Equation (2)	Exp	Δ
1	912	960	48	1824	1824	0	2736	2744	8
2	936	980	44	1872	1860	−12	2808	2816	8
3	948	1024	76	1896	1880	−16	2844	2848	4
4	900	872	−28	1800	1852	52	2700	2688	−12
5	880	—	—	1760	1760	0	2640	2624	−16
6	880	—	—	1760	1760	0	2640	2624	−16
7	874	—	—	1748	1752	4	2622	2576	−46
8	860	—	—	1720	—	—	2580	2560	−20

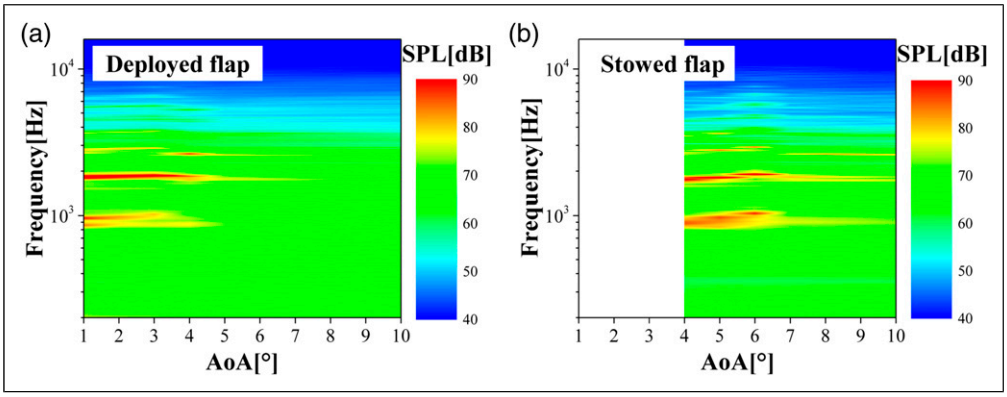

Figure 7. Sound Pressure Level contour maps of far-field noise for high-lift configurations (experimental results).

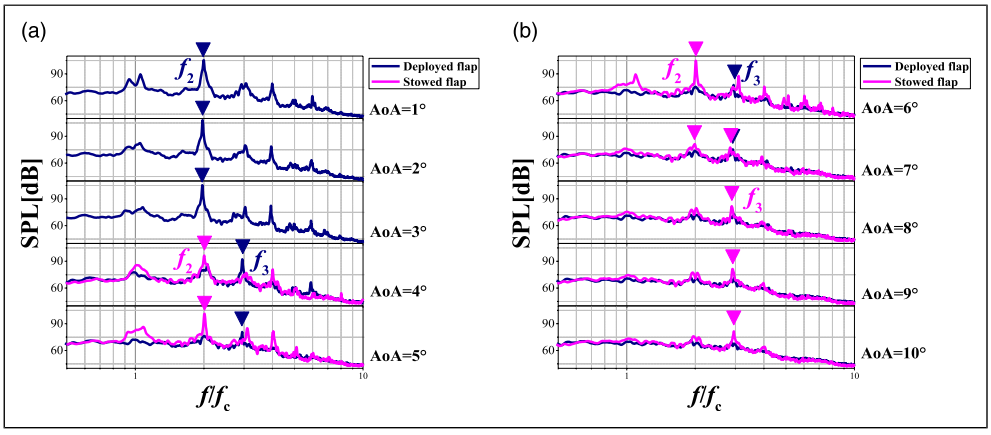

Figure 8. Far-field noise spectra for high-lift configurations (experimental results).

zone, and the reattachment point is farther away from the upper trailing edge of the slat. Hence, the variation trend of the shear layer lengths between the cusp and the reattachment position along the mean flow streamline following the mean shear layer, L_v, can be expressed as

$$L_v(deployed\ flap) < L_v(stowed\ flap) \tag{6}$$

In addition, flow in the gap is much faster than that in the recirculation zone, and momentum is transferred to the recirculation zone by shearing. It can be seen from Figure 9, that the closer the mean flow streamline is to the recirculation zone, the lower the mean convection velocity is. Furthermore, the flap deployed increases the local effective AoA of the leading-edge slat. The stagnation point is located on the lower surface of the leading edge of the slat, and the flow from the stagnation point to the cusp is subjected to a small positive pressure gradient. The flow is slowly accelerating along the lower surface of the slat. For the high-lift configuration with a stowed

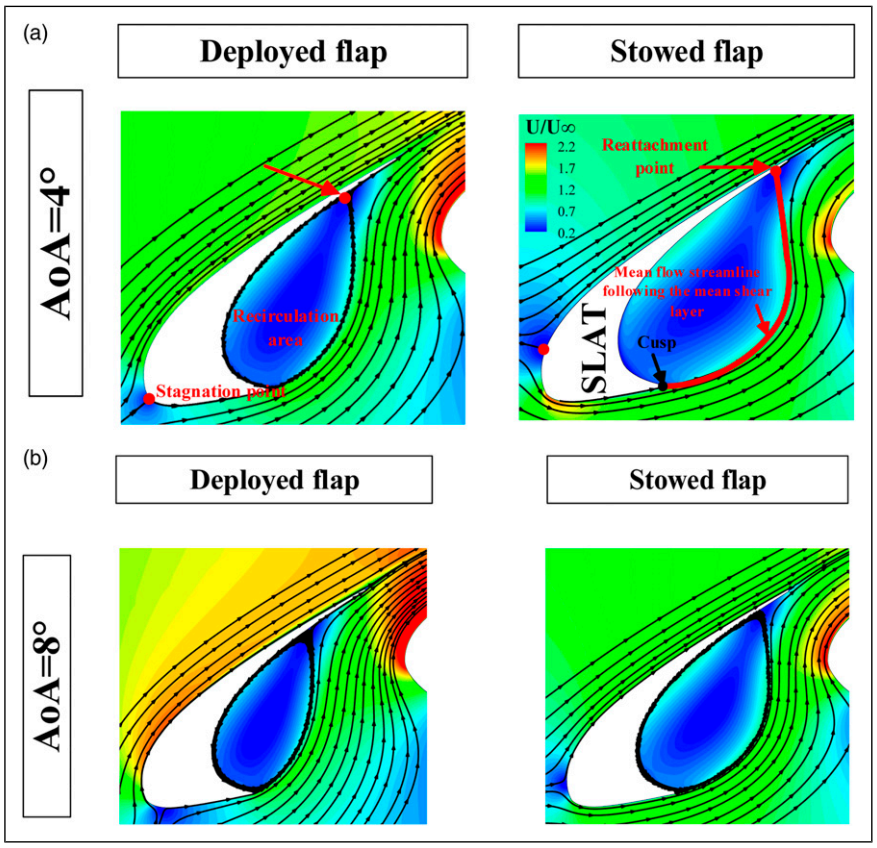

Figure 9. (a and b) Velocity contour in the vicinity of the slat and mean flow streamlines (calculation results).

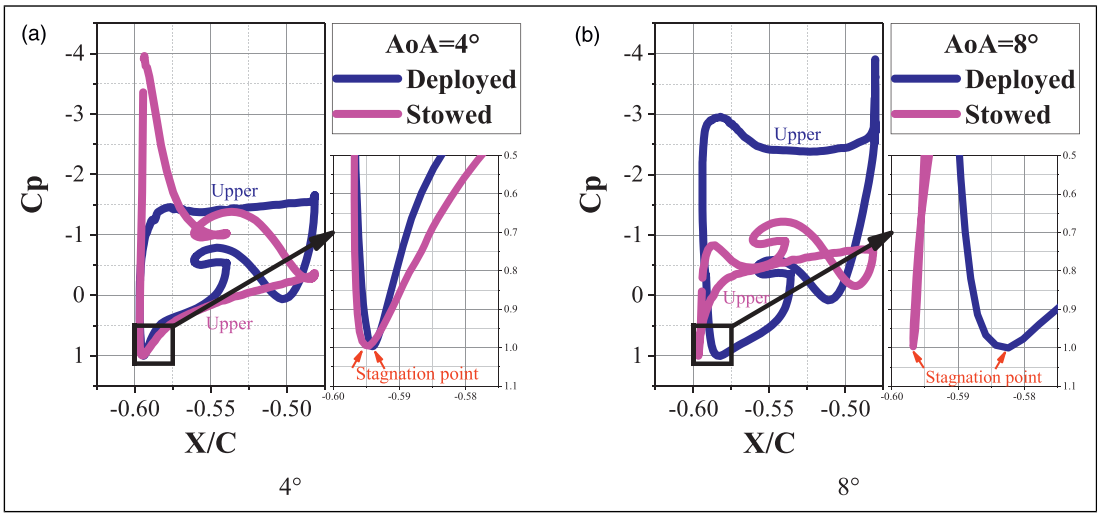

Figure 10. Pressure distribution of the slat (calculation results).

flap, the stagnation point is located on the upper surface and the suction peak is located on the lower surface. The flow is quickly accelerating and then decelerating from the stagnation point to the cusp, for the reason that the flow subjected to a positive pressure gradient first and then, a large negative pressure gradient occurs.

Figure 11 shows the velocity magnitude evolution along the mean flow streamline following the mean shear layer. According to Ref. 9, the mean convection velocity, U_v, is approximated by the mean plateau value of the velocity, U. It should be mentioned that the horizontal and vertical coordinates in Figure 10 are dimensionless, using L_v and U_{max}, respectively.

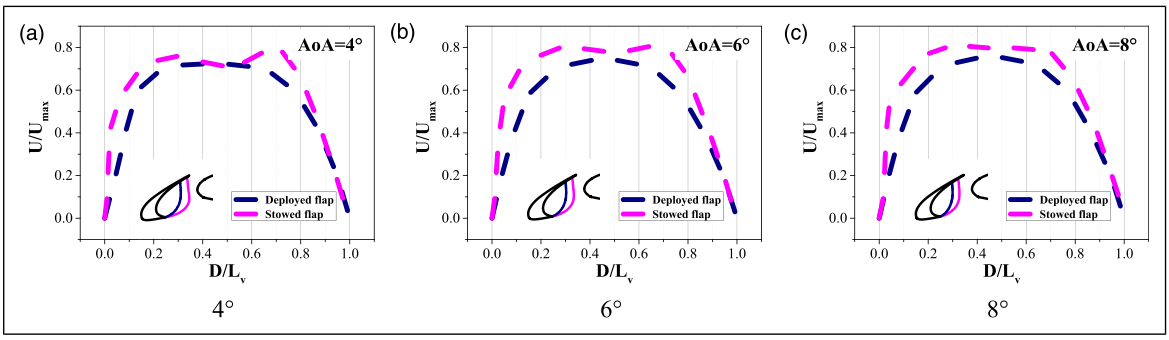

Figure 11. Velocity magnitude evolution along the mean flow streamline following the mean shear layer (calculation results).

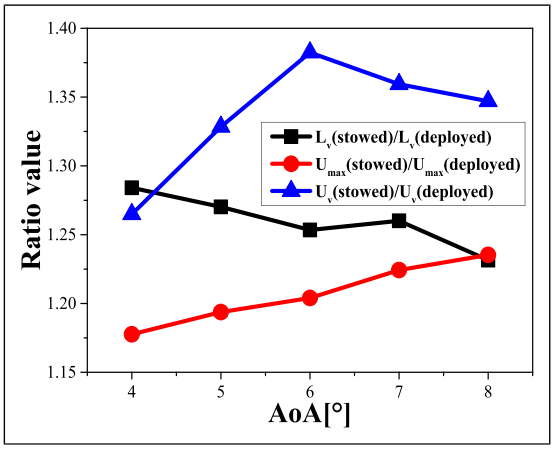

Figure 12. Ratio values of flow field parameters when the flap is deployed and stowed (calculation results).

Hence, the variation trend of the mean convection velocity, U_v, maximum velocity in the separating boundary layer, U_{max} and the ratio of the two, K_v, can be expressed as

$$\begin{cases} U_v(deployed\ flap) \ll U_v(stowed\ flap) \\ U_{max}(deployed\ flap) < U_{max}(stowed\ flap) \\ K_v(deployed\ flap) < K_v(stowed\ flap) \end{cases} \quad (7)$$

The ratio the of values of L_v, U_v, and U_{max} when the flap is stowed to that when the flaps are deployed is shown in Figure 12. It can be seen that the variation trends are same to equation (6) and (7). These ratios are all greater than 1, with U_v having the largest ratio. This shows that at the same AoA, the values of these parameters increase as the flap is deployed.

It can be seen from Figure 13 that the boundary layer develops from the stagnation point to the cusp. Due to the flap deployed, the local effective AoA of the leading-edge slat increases, the stagnation point is located on the lower surface and the development distance of the boundary layer is shorter along the lower surface of the leading edge of the slat. In addition, as mentioned above, the pressure difference is lower during boundary layer development for the three-element high-lift configuration. These factors result in a thinner separating boundary layer near the cusp. The velocity profiles following the normal direction of the separating boundary layer are shown in Figure 14. Clearly, the separating boundary layer is thinner and the maximum velocity in the separating boundary layer is lower for the high-lift configuration with a flap being deployed.

Hence, the variation trend of the separating boundary layer thickness, δ, can be expressed as

$$\delta(deployed\ flap) < \delta(stowed\ flap) \quad (8)$$

Figure 15 shows the ratio values of flow parameters related to the primary mode before and after the flap deployment. At different AoAs, the variation trend of the three parameters L_v, δ, K_v, before and after the flap is deployed, can be seen from Figure 15, among which the relative change rate of the parameter δ is the largest. Compared with δ, the boundary layer thickness, the relative change rates of the other two parameters are small, especially at AoAs below 6°. Therefore, the variation trend of $L_v/(\delta \cdot K_v)$ depends largely on δ.

Figure 16 shows the relationship between the value of the ratio and the primary mode of self-excited oscillation. The solid points represent the cases for ModeII, the open points pertain to the cases of ModeIII, and the center points represent the cases for the mode transition phase. At the same AoA (4°), ModeII is the main self-excited oscillation mode for the high-lift configuration with a flap stowed, when n is approximately equal to 2. ModeIII is the main self-excited oscillation mode for the high-lift configuration with a flap deployed, when n is approximately equal to 3. It can be seen that the ratio, $L_v/(\delta \cdot K_v)$, becomes larger no whether the AoA increases or the flap is deployed. As mentioned above, all three parameters, L_v, δ, and K_v, decrease when the flap is deployed, among which δ has the largest relative change rate. And δ is inversely proportional to the ratio, $L_v/(\delta \cdot K_v)$. When the flap is deployed, the ratio, $L_v/(\delta \cdot K_v)$ increases, which is proportional to the ratio between the vortex shedding frequency and the self-excited oscillation frequency. This means that during a self-excited oscillation period, the quantity of vortices, contained simultaneously in the free shear layer and impinging upon the lower surface of the

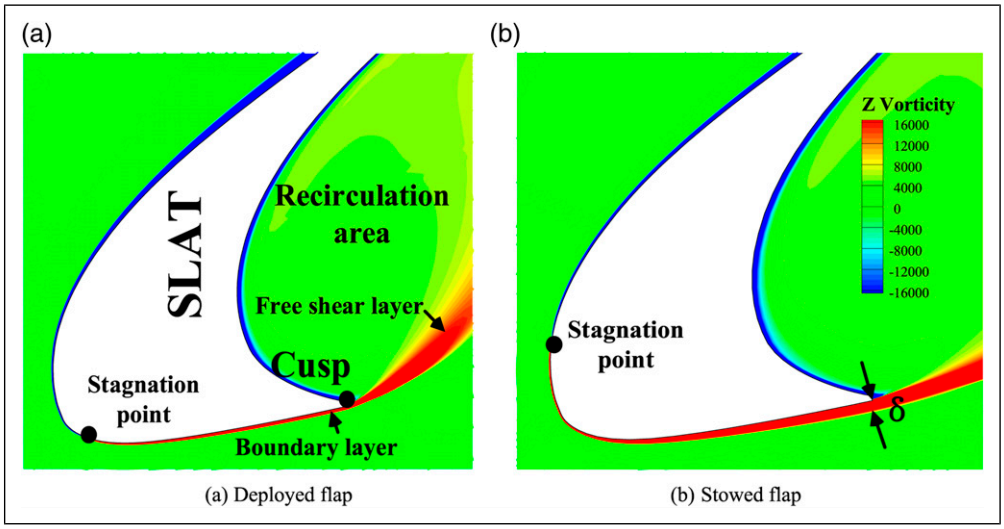

Figure 13. Z vorticity contour around the cusp of the slat at an AoA of 6°(calculation results).

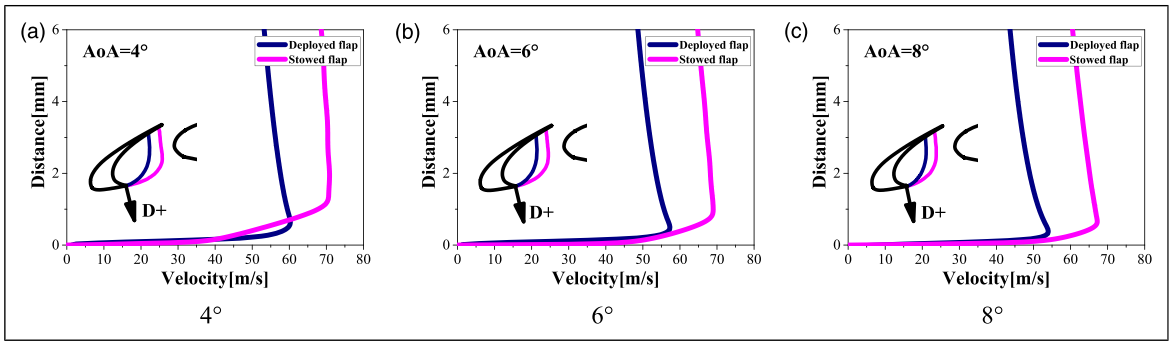

Figure 14. Velocity profiles following the normal direction of the separating boundary layer near the cusp of the slat (calculation results).

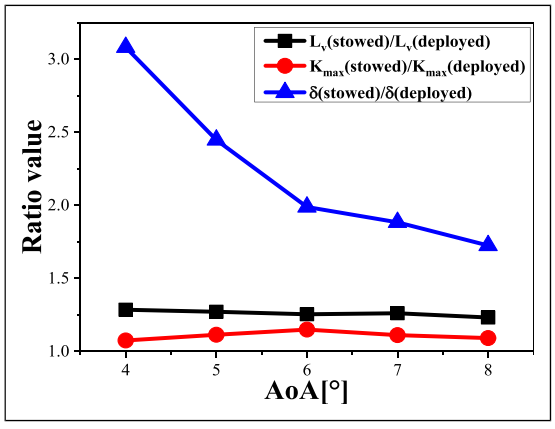

Figure 15. Ratio values of flow parameters related to the primary mode (L_v, δ, K_v) before and after the flap deployment (calculation results).

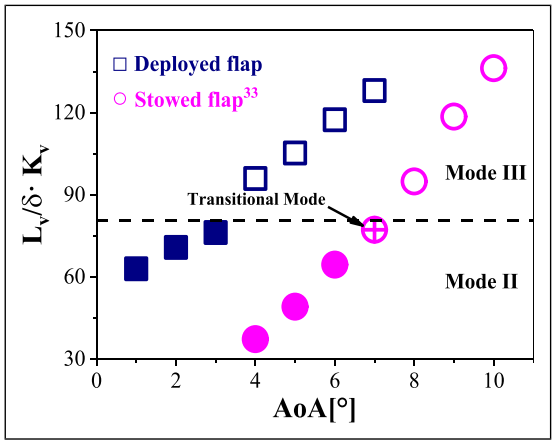

Figure 16. The relationship between the value of the ratio $L_v/(\delta \cdot K_v)$ and primary mode of self-excited oscillation (experimental and calculation results).

upper trailing edge of the slat, increases, which further causes the primary mode to switch to a high one.

Conclusions

Aero-acoustic experiments on a two-dimensional high-lift configuration model with and without a flap, respectively, were carried out in the D5 aero-acoustic wind tunnel at Beihang University. The purpose of this paper has been to study the far-field noise characteristics of the leading-edge slat of high-lift configurations with and without a deployed trailing-edge flap to evaluate the noise characteristics, while eliminating the noise interference of the trailing-edge flap.

(1) Far-field noise results show that low to mid frequency tonal noise generated by self-excited oscillation within the slat cove is dominant for both two-element and three-element high-lift configurations. Whether the flap is deployed or not does not substantially affect the corresponding frequencies of the low to mid frequency tonal noise. The maximum intensity of these tones is basically at the same level. However, the main mode of self-excited oscillation is affected by whether the flap is deployed or not. At the same AoA (from 4° to 6°), ModeIIis the main self-excited oscillation mode for the two-element high-lift configuration; ModeIII is so for the three-element high-lift configuration.

(2) Analyzing further the relationship between the primary mode of self-excited oscillation and local flow information of the slat, it is found that, compared with the high-lift configuration with a flap being stowed, the local effective angle of attack of the leading-edge slat increases when the flap is deployed. This further leads to the change of the flow field characteristics near the slat. At the same angle of attack of incoming flow, the shear layer length between the cusp and the reattachment position, L_v, the separating boundary layer thickness, δ, and the ratio of average vortex convection velocity along the shear layer to the maximum velocity in the shear layer near the cusp, K_v, all decrease when the flap is deployed. Since the relative change rate of δ (the slope of $\delta_{stowed}/\delta_{deploded}$) is much larger than that of the other two in the range of angles of attack studied in this paper, the variation trend of $L_v/(\delta \cdot K_v)$ depends largely on δ. The ratio, $L_v/(\delta \cdot K_v)$, is proportional to the ratio between the vortex shedding frequency and the self-excited oscillation frequency, which is proportional to the number of the primary mode, n_p. Therefore, the primary mode of the self-excited oscillation within the slat cove switches to a high one when the flap is deployed.

Declaration of conflicting interests

The author(s) declared no potential conflicts of interest with respect to the research, authorship, and/or publication of this article.

Funding

The author(s) disclosed receipt of the following financial support for the research, authorship, and/or publication of this article: This work was supported by the National Natural Science Foundation of China (Grant No. 11502012, 11850410440, 11772033 and 11721202).

ORCID iD

Hao Guo https://orcid.org/0000-0002-2557-1972

References

1. Dobrzynski W. Almost 40 years of airframe noise research: what did we achieved. *J Aircraft* 2010; 47(2): 353–367.
2. Xu CC and Cho HM. Analysis on the noise reduction of engine with air intake resonator in engine intake system. *Int J Eng Technol* 2018; 10(1): 149–153.
3. Guo YP and Joshi MC. Noise characteristics of aircraft high lift systems. *J Aircr* 2003; 41(7): 1247–1256.
4. Guo YP, Yamamoto KJ and Stoker RW. Component-based empirical model for high-lift system noise prediction. *J Aircr* 2003; 40(5): 914–922.
5. Pagani CC, Jr., Souza DS and Medeiros MAF. Slat noise: aeroacoustic beamforming in closed-section wind tunnel with numerical comparison. *AIAA J* 2016; 54(No. 7): 2100–2115.
6. Pagani CC, Souza DS and Medeiros MAF. Experimental investigation on the effect of slat geometrical configurations on aerodynamic noise. *J Sound Vibration* 2017; 394: 256–279.
7. Ma Z and Zhang X. Numerical investigation of broadband slat noise attenuation with acoustic liner treatment. *AIAA J* 2009; 47(12): 2812–2820.
8. Kuo BC and Sarigul-Klijn N. Conceptual study of micro-tab device in airframe noise reduction: (I) 2D computation. *Aerospace Sci Technol* 2010; 14(5): 307–315.
9. Amaral FRD, Himeno FHT, Pagani CDC, et al. Slat noise from an MD30P30N airfoil at extreme angles of attack. *AIAA J* 2017; 56: 1–15.
10. Imamura T, Enomoto S, Yokokawa Y, et al. Three-dimensional unsteady flow computations around a conventional slat of high-lift devices. *AIAA J* 2008; 46(No. 5): 1045–1053.
11. Khorrami MR, Berkman ME and Choudhari M. Unsteady flow computations of a slat with a blunt trailing edge. *AIAA J* 2000; 38(11): 2050–2058.
12. Kolb A, Faulhaber P, Drobietz R, et al. Aeroacoustic wind tunnel measurements on a 2D high-lift configuration. In: 13th AIAA/CEAS Aeroacoustics Conference (28th AIAA Aeroacoustics Conference), Rome, Italy, 2013
13. Terracol M, Manoha E and Lemoine B. Investigation of the unsteady flow and noise generation in a slat cove. *AIAA J* 2017; 54(2): 1–21.
14. Rossiter JE. *Wind-tunnel experiments on the flow over rectangular cavities at subsonic and transonic speeds*. Aeronautical Research Council Reports and Memoranda, 1966. Ministry of Aviation; Royal Aircraft Establish-ment; RAE Farnborough, 1964.
15. Pereira LTL, Rego LF, Catalano FM, et al. Experimental slat noise assessment through phased array and hot-film anemometry measurements. In: 2018 AIAA Aerospace Sciences Meeting, Kissimmee, Florida,2018

16. Li L, Liu P, Guo H, et al. Aeroacoustic measurement of 30P30N high-lift configuration in the test section with Kevlar cloth and perforated plate. *Aerosp Sci Technol* 2017; 70: 590–599.
17. van Dam CP. The aerodynamic design of multi-element high-lift systems for transport airplanes. *Prog Aerospace Sci* 2002; 38: 101–144.
18. Zhang Y, Adam O'N, Cattafesta L, et al. Assessment of noise reduction concepts for leading-edge slat noise. In: 2018 AIAA/CEAS Aeroacoustics Conference, Atlanta, Georgia, 2018.
19. Murayama M, Yokokawa Y and Ura H. *Experimental study of slat noise from 30P30N three-element high-lift airfoil in JAXA Kevlar-wall low-speed wind tunnel*. Atlanta: AIAA/CEAS Aeroacoustics ConferenceGeorgia,2018, (accessed 2018).
20. Liu P, Xing Y, Guo H, et al. Design and performance of a small-scale aeroacoustic wind tunnel. *Appl Acoust* 2017; 116: 65–69.
21. Devenport WJ, Burdisso RA, Borgoltz A, et al. The Kevlar-walled anechoic wind tunnel. *J Sound Vibration* 2013; 332: 3971–3991.
22. Pascioni KA and Cattafesta LN. An aeroacoustic study of a leading-edge slat: beamforming and far field estimation using near field quantities. *J Sound Vibration* 2018; 429: 224–244.
23. Lu W, Liu P and Guo H. Experimental study on aerodynamic noise characteristics of high-lift configuration with variable gap leading-edge slat. *The Journal of the Acoustical Society of America* 2018; 144(3): 1708–1708.
24. Campobasso S, Yan M, Bonfiglioli A, et al. Low-speed preconditioning for strongly coupled integration of Reynolds-averaged Navier–Stokes equations and two-equation turbulence models. *Aerosp Sci Technol* 2018; 77: 286–298.
25. Qu F and Sun D. Investigation into the influences of the low-speed flows' accuracy on RANS simulations. *Aerosp Sci Technol* 2017; 70: 578–579.
26. Lu W, Tian Y and Liu P. Aerodynamic optimization and mechanism design of flexible variable camber trailing-edge flap. *Chin J Aeronautics* 2017; 30(3): 988–1003.
27. Chin VD, Peters DW, Spaid FW, et al. Flow field measurements about a multi-element airfoil at high Reynolds numbers. In: 24th AIAA fluid dynamics conference. Reston, VA, Aug 22: AIAA, 1993.
28. Choudhari MM and Khorrami MR. Effect of three-dimensional shear-layer structures on slat cove unsteadiness. *AIAA J* 2007; 45(9): 2174–2186.
29. Ziada S and Rockwell D. Oscillations of an unstable mixing layer impinging upon an edge. *J Fluid Mech* 1982; 124(124): 307–334.
30. Gharib M and Roshko A. The effect of flow oscillations on cavity drag. *J Fluid Mech* 1987; 177: 501–530.
31. Ziada S and Rockwell D. Generation of higher harmonics in a self-oscillating mixing layer-wedge system. *AIAA J* 1982; 20(2): 196–202.
32. Lu W, Liu P, Guo H, et al. Investigation on tones due to self-excited oscillation within the leading-edge slat cove at different incoming flow speeds. *Appl Acoust* 2019; 155(2019): 232–239.
33. Lu W, Liu P, Guo H, et al. Investigation on tones due to self-excited oscillation within leading-edge slat cove at different angles of attack: frequency and intensity[J]. *Aerospace Sci Technol* 2019; 91(2019): 59–69.